Turbulent flame acceleration and deflagration-to-detonation transitions in ethane–air mixture 🄴🄿

Jinzhou Li ⓘ ; Sven Van Loo ⓘ ; Junfeng Yang ✉ ⓘ ; Andrzej Pekalski

Check for updates

View Online   Export Citation

Turbulent flame acceleration and deflagration-to-detonation transitions in ethane–air mixture ⓔⓟ

Jinzhou Li,[1] ⓘⒹ Sven Van Loo,[2] ⓘⒹ Junfeng Yang,[1,a] ⓘⒹ and Andrzej Pekalski[3]

AFFILIATIONS

[1]School of Mechanical Engineering, University of Leeds, Leeds LS2 9JT, United Kingdom
[2]Department of Applied Physics, Ghent University, Ghent, Belgium
[3]Shell Research Limited, London, United Kingdom

[a]Author to whom correspondence should be addressed: J.Yang@leeds.ac.uk

ABSTRACT

The deflagration-to-detonation transition (DDT) poses significant risks in the oil, gas, and nuclear industries, capable of causing catastrophic explosions and extensive damage. This study addresses a critical knowledge gap in understanding the DDT of ethane–air mixtures on a large scale, amid increasing industrial utilization and production of ethane. A novel computational framework is introduced, utilizing the finite-volume code named Morris Garages, which incorporates reactive compressible Navier–Stokes equations, adaptive mesh refinement, and correlations of turbulent burning velocities. This model integrates the most recent data on laminar and turbulent burning velocities for premixed ethane–air mixtures, simulating flame acceleration and DDT within a two-dimensional large-scale setting, measuring 21 m in length and 3 m in height, with obstacles mimicking pipe congestion. Two mixture scenarios, lean and near-stoichiometric, are analyzed to evaluate the effects of equivalence ratios on flame propagation and DDT. The simulations, validated against large-scale experimental data from Shell, show reasonable agreement and provide critical insights into the onset conditions of DDT, such as temperature, pressure, flame speed, and turbulent kinetic energy. Furthermore, the ξ–ε detonation peninsula diagram is utilized to explore autoignition and detonation behaviors in ethane–air mixtures.

NOMENCLATURE

a Acoustic velocity (m/s)
c Progress variable
E Density-weighted average total energy
K Karlovitz stretch factor
k Turbulent kinetic energy (m^2/s^2)
L Intergral length scale (m)
P Pressure (MPa)
P_0 Datum atmospheric pressure (MPa)
Pr Prandtl number
r_0 Hot spot radius (m)
R Reaction constant
S_E Source term for the energy
S_c Source term for the progress variable
T Temperature (K)
t Time (s)

U Dimensionless parameter with the ratio of $\frac{u_t}{u_k'}$
u Velocity vector (m/s)
u' RMS turbulent velocity (m/s)
u_k' Effective rms turbulent velocity (m/s)
u_l Unstretched laminar burning velocity (m/s)
u_t Turbulent burning velocity (m/s)
x Mesh cell size (m)

Greek symbols

α Numerical constant, thermal diffusivity (m^2/s)
β Numerical constant
γ Ratio of specific heats
δ_t Turbulent flame thickness (m)
ε Ratio of $\frac{r_0}{a\tau_e}$, excitation factor; turbulent dissipation rate (m^2/s^3)
ν unburned gas kinematic viscosity (m^2/s)

ξ	Ratio of u_a/a
ξ_l	Lower limits of detonation peninsula
ξ_u	Upper limits of detonation peninsula
ρ	Density (kg/m^3)
ρ_b	Burned gas density (kg/m^3)
ρ_u	Unburned gas density (kg/m^3)
τ_e	Chemical excitation time (μs)
τ_i	Ignition delay time (ms)
τ	Stress tensor (N/m^2)
μ	Molecular viscosity [kg/(m s)]
μ_t	Turbulent viscosity [kg/(m s)]
ϕ	Equivalence ratio
ω	Turbulent dissipation rate (m^2/s^3)
Λ	Eigenvalue value

I. INTRODUCTION

The accidental explosions of fuel–air mixtures within the oil, gas, and nuclear industries pose significant risks to both life and property. These explosions can escalate into severe detonations via the deflagration-to-detonation transition (DDT), a phenomenon where, once initiated, detonations rapidly consume the entire detonable mixture. Characterized by propagation speeds approximately 1800 m/s (supersonic) and pressures surpassing 18 bars, such detonation waves present severe threats. The supersonic propagation of the reaction wave and the intense overpressure not only endanger lives but also cause extensive damage to properties.

To unravel the mechanisms of DDT on a large scale, comprehensive experimental research has been conducted, particularly focusing on hydrogen, methane, and ethane.[1–5] These studies have utilized various obstacles to simulate the congested environments typical of industrial facilities, aiming to accelerate flame speed and foster the formation of turbulent shock–flame complexes. Additionally, sophisticated instrumentation such as pressure transducers and high-speed cameras have been deployed to meticulously capture data on overpressure and the velocity of turbulent flame propagation. Recent breakthroughs in computational technology have also paved the way for employing computational fluid dynamics (CFD) software or codes, alongside chemical kinetics mechanisms, to simulate the intricate behavior of turbulent flame propagation and DDT.[6–12] This computational approach has generated detailed insights into critical parameters such as temperature, pressure, density, flame speed, and the distribution of flow fields, which are instrumental in understanding the process of flame acceleration leading to DDT. The focus of these investigations, particularly in numerical simulations, has been on hydrogen, methane, and their mixtures. These studies delineate DDT into three distinct phases: the initial acceleration of the flame as it encounters obstacles, which significantly contributes to turbulence growth; the critical transition phase to detonation, triggered by localized conditions of heightened temperature and pressure; and finally, the propagation of detonation.

Ethane is an important petrochemical product, primarily used as a feedstock in the petrochemical industry to produce ethylene, which is further processed into various chemicals and plastics.[13] Ethane is the second-largest component in natural gas, with its concentration ranging between 0.5% and 13.3% by volume.[13] The increasing production, storage, and utilization of ethane have highlighted the importance of a thorough understanding of safety measures. This is crucial, especially

considering the potential risks associated with DDT, underscoring the need for advanced knowledge in managing and harnessing ethane as a reliable and safe energy source.

Despite the extensive research on DDT, a few studies have yet presented large-scale simulations of turbulent flame acceleration and DDT specifically for ethane–air mixtures. This gap in the literature is likely due to the limited availability of measured laminar and turbulent burning velocities for ethane, which are crucial inputs for combustion model. Additionally, the complex nature of ethane chemical kinetics mechanism, characterized by a large number of dominant reactions and species, renders such simulations computationally expensive when detailed kinetic mechanisms are applied. Nevertheless, the recent experimental work yields measured data for laminar premixed ethane–air[14] and turbulent premixed ethane–air burning velocities.[15] These valuable experimental data enable the incorporation of accurately measured burning velocity inputs into large-scale simulations of ethane–air turbulent flame propagation and DDT.

The storage safety concerns and fire hazards associated with ethane have underscored the importance of simulating its DDT behavior on a large scale. This study proposes a novel framework integrating CFD coding with a progress variable, which includes a measured turbulent burning velocity correlation from a fan-stirred combustion vessel, to simulate ethane–air flame propagation and DDT. Furthermore, this research integrates the Zel'dovich hot spot theory[16] and the ξ–ε detonation peninsula diagram[17] to meticulously quantify ignition regimes, including subsonic autoignition and developing detonation for ethane–air mixtures, aiming to pinpoint conditions under which DDT occurs. The framework employs the finite volume code named Morris Garages (MG) developed by Mantis Numerics Ltd.,[18] which leverages a second-order Godunov–Riemann scheme, adaptive mesh refinement (AMR), and Reynolds-averaged Navier–Stokes (RANS) techniques to enhance the precision and efficiency of the simulations. The turbulent flame propagation and DDT for ethane–air simulation in congested rig are presented, compared, and validated with Shell large-scale experimental work.[2] Additionally, the study delves into the impact of equivalence ratio variations and different turbulence models on the simulation results.

II. EXPERIMENTAL AND NUMERICAL SETUP
A. Experimental setup

In order to validate the simulation approach, it is critical to review the large-scale experimental study of ethane–air mixture is conducted by Pekalski et al.[2] in a congested rig in present study. This large-scale experimental study aimed to investigate whether the ethane–air can lead to the transition to detonation. The experimental work has been conducted within a steel structure, approximately 21 m in length, 6 m in width, and 3 m in height, stationed on a concrete pad. The congested area contains steel pipes in an arrangement of 16 × 16 by 8 pipes, each of which had a diameter of approximately 76 mm and were set at a pitch of 342 mm. The congested area was a regular cuboid array of vertical and horizontal steel pipes with a uniform dimension of about 5.2 m in length, 5.2 m in width, and 2.6 m in height. A single polythene sheet, covering the steel frame, was utilized to contain the ethane–air mixture before igniting. In this experiment, the ignition was achieved by an electrical spark, which was located at the edge along the central line of congestion pipe line.

During the test rig's filling process, high-purity ethane was used, with an infrared analyzer employed to monitor and ensure the uniformity of the ethane–air mixture. It was confirmed that the equivalence ratio for this mixture is near stoichiometric, around 1.05. The temperature and pressure of the ethane–air mixture are 300 K and 0.1 MPa, respectively. Two high-speed video cameras were also used to monitor the flame progression and measured the reaction wave propagation speed ran at typically 3000 fps. The development of overpressure within the test rig was measured using 11 pressure transducers, which were distributed over a length of 21 m and installed flush with ground level.

B. Mathematical model

The numerical approach addresses the two-dimensional (2D) fully compressible, reactive Navier–Stokes (NS) equations along with ensemble-averaged, density-weighted transport equations for mass, momentum, total energy, and a reaction progress variable. This method employs a second-order Godunov–Riemann scheme, derived from Ref. 18, which is well-suited for solving the Euler equations in computational fluid dynamics. This approach is particularly effective in capturing shocks and discontinuities, crucial for accurately simulating flame dynamics and transitions to detonation processes.

The governing equations are as follows:
Mass conservation

$$\frac{\partial \rho}{\partial t} + \nabla \cdot (\rho u) = 0. \tag{1}$$

Momentum conservation

$$\frac{\partial (\rho u)}{\partial t} + \nabla \cdot (\rho u \otimes u) = -\nabla \cdot P + \nabla \cdot \tau. \tag{2}$$

Energy conservation

$$\frac{\partial (\rho E)}{\partial t} + \nabla \cdot (\rho u E + P u) = \nabla \cdot \left[u\tau + \left(\frac{\mu + \mu_T}{P_r} \right) \frac{\gamma}{\gamma - 1} \nabla \cdot T \right] + \rho S_E. \tag{3}$$

Stress tensor

$$\tau = 2(\mu + \mu_T)(\nabla \cdot u) - \frac{2}{3} \mu_T (\nabla \cdot u) I - \frac{2}{3} \rho k I. \tag{4}$$

In above expressions, ρ represents the density of the fluid, u denotes the velocity vector, P signifies the pressure, and T indicates the temperature of the mixture. The Prandtl number, P_r, is defined as the ratio of kinematic viscosity, ν, to thermal diffusivity, α. The ratio of specific heats is represented by γ. The symbol, μ, represents molecular viscosity, while μ_T denotes the turbulent viscosity. The standard k–ε[19] turbulent model is implemented in current simulation. The k–ε model is particularly effective in high Reynolds number turbulent flows, as reported by the simulation study of Ref. 20, making it suitable for simulations involving high-speed turbulent flame propagation and detonation transitions. The model is relatively simple to implement and solve, making it a good choice for large-scale simulations. However, the k–ε model has limitations, particularly in treating boundary layers. To address this issue, a level 4 AMR mesh is used to refine mesh density near flame front, walls, and obstacles, thereby enhancing the simulation accuracy in these critical areas.

The turbulent viscosity is calculated as $0.09 \frac{\rho k^2}{\varepsilon}$ for k–ε model. The term k and ε represents the turbulent kinetic energy and the turbulent dissipation rate, respectively. The total energy density E is defined as $0.5(u^2) + \frac{P}{(\gamma-1)\rho}$. The source term for the energy, S_E, is defined as $S_c \left(\frac{P}{\rho_u} \right) \left(\frac{\rho_u}{\rho_b} - 1 \right) \frac{\gamma}{\gamma-1}$. Here, ρ_u is the unburned gases density and ρ_b is the burned gases density.

The interaction between the turbulence and premixed combustion was evaluated by Catlin et al.[21] This method incorporates the experimental measured turbulent burning velocity correlation with effects of kinetics and turbulence influences upon the turbulent burning velocity of flame, while remaining a realistic flame thickness throughout the computation. The conservation equations representing a reaction progress variable of the mixture are defined as follows:

$$\frac{\partial}{\partial t}(\rho c) + \nabla \cdot (\rho u c) = \nabla \cdot (\Gamma_c \nabla c) + \rho S_c. \tag{5}$$

With diffusivity coefficient, $\Gamma_c = (\mu + \mu_T)/\sigma_c$. In addition, the reaction progress variable is defined as follows:

$$c = 1 - (Y_f / Y_{f,o}). \tag{6}$$

The progress variable is used to describe the flame front and so that $c = 0$ is the unburned mixture and $c = 1$ is the burned mixture. The source term of the progress variable in Eq. (5) can be written as

$$\rho S_c = \rho R c^4 (1 - c) \left(\frac{\rho_u}{\rho_b} \right)^2. \tag{7}$$

The reaction rate constant, R, is a function of the turbulent burning velocity and turbulent flame thickness and expressed as

$$R = u_t \Lambda_2 / (\delta_t \Lambda_1), \tag{8}$$

where flowing the work of Catlin et al.,[21] the eigenvalues Λ_1 and Λ_2 are suggested as 0.346 and 3.575, respectively. The symbol δ_t is the turbulent flame thickness and is taken to the turbulence length scale given by

$$\delta_t = l = C_\mu^{3/4} k^{3/2} / \varepsilon, \tag{9}$$

where C_μ is the constant with the value of 0.09.

C. Turbulent burning velocity correlation of ethane–air

Equation (8) indicates that calculating the reaction constant necessitates a detailed understanding of the turbulent burning velocity for ethane–air mixtures. Experimental values for turbulent burning velocity, alongside measurements of temperature, pressure, equivalence ratio, and root mean square (RMS) turbulent velocity for ethane–air, have been documented in a fan-stirred combustion vessel as found in Ref. 15. This numerical study selects two equivalence ratios: near-stoichiometric ($\phi = 1.05$) to match the conditions of large-scale ethane explosion experiments reported in Ref. 2, and lean ($\phi = 0.8$) to investigate the impact of equivalence ratio on turbulent flame propagation and DDT. Although the study in Ref. 15 did not provide experimental turbulent burning velocities at an equivalence ratio of 1.05, it includes data for both laminar and turbulent velocities at stoichiometric conditions. The minor increase in equivalence ratio to 1.05 is

TABLE I. Value of constant factors for ethane–air mixtures at $\phi = 1$ and $\phi = 0.8$.

	$\phi = 1$	$\phi = 0.8$
α	0.36	0.35
β	−0.29	−0.32
β_P	0.2	0.18
β_T	0.5	0.25
β_{Tl}	1.55	1.39
β_{Pl}	−0.24	−0.3
β_{Tv}	1.74	1.72

unlikely to significantly impact laminar/turbulent burning velocities. As such, the correlation for turbulent burning velocities at equivalence ratios of 1 and 0.8 for ethane–air mixtures is applied in the analysis.

In this numerical analysis, a novel approach to estimating turbulent burning velocity for ethane–air mixtures is proposed, building on the foundational work by Bradley et al.[22] This approach introduces a correlation emphasizing the role of turbulence in enhancing flame surface wrinkling and the influence of strain rate on turbulent flames. The proposed correlation incorporates two dimensionless parameters: U that represents the ratio of turbulent burning velocity, u_t to the effect rms turbulent velocity, u'_k, and the Karlovitz stretch factor, K. Additionally, it accounts for the effects of temperature and pressure as follows:

$$U = \frac{u_t}{u'_k} = \alpha K^\beta \left(\frac{P}{0.1}\right)^{\beta_P} \left(\frac{T}{300}\right)^{\beta_T} \tag{10}$$

with the initial unburned pressure, P, in MPa and temperature, T, in K. Here, α and β are constants whose values depend on the mixture type and equivalence ratio, while β_P and β_T represent the factors for pressure and temperature effects, respectively. The Karlovitz stretch factor is defined by the equation:

$$K = 0.25 \left(u'/u_l\right)^2 \left(u'L/\nu\right)^{-0.5}, \tag{11}$$

where u_l denotes the laminar burning velocity of the ethane–air mixture under specific T and P conditions:

$$u_l = u_{l0}(T/300)^{\beta_{Tl}}(P/0.1)^{\beta_{Pl}}, \tag{12}$$

u_{l0} is the laminar burning velocity at 300 K and 0.1 MPa. This value, along with the factors β_{Tl} and β_{Pl} that represent the influence of temperature and pressure on the laminar burning velocity, respectively, is detailed in Table I. The term u' denotes the rms turbulent velocity, and L indicates turbulent length scale, and ν is the kinematic viscosity of ethane–air mixture. The initial integral length scale, L, is given as 2 cm and consistent with the combustion vessel. The kinematic viscosities, ν, of ethane–air at conditions of T and P expressed as

$$\nu = \nu_0(T/300)^{\beta_{Tv}}(P/0.1)^{-1}, \tag{13}$$

where ν_0 is the kinematic viscosity at 300 K and 0.1 MPa, sourced from GASEQ.[23] The constant β_{Tv} is the temperature effect factor on the kinematic viscosity. The best-fit values for the constant factors mentioned above, applicable to ethane–air mixtures at equivalence ratios of $\phi = 1$ and $\phi = 0.8$, are detailed in Table I below. The standard $k - \varepsilon$ model is implemented in this study, and following the study of Catlin et al.,[21] the rms turbulent velocity, u', is expressed related to the turbulence kinetic energy, k:

$$u' = (2k/3)^{0.5}. \tag{14}$$

Given measurements of turbulent burning velocities at a radial distance $r_{sch} = 30$ mm, within this radius, $u'_k = 0.7u'$. This relationship allows for the reformulation of Eq. (14) as follows:

$$u'_k = 0.7(2k/3)^{0.5}. \tag{15}$$

Figure 1 illustrates the comparison between measured turbulent burning velocities of ethane–air under various conditions from Ref. 15 (depicted with symbols) and the outcomes of the correlation from Eq. (10) (shown with solid lines) for two cases of equivalence ratios, 1.0 on the left and 0.8 on the right. The correlation for both equivalence ratios yield high fitting coefficients of determination, $R^2 = 0.99$ and 0.96, respectively.
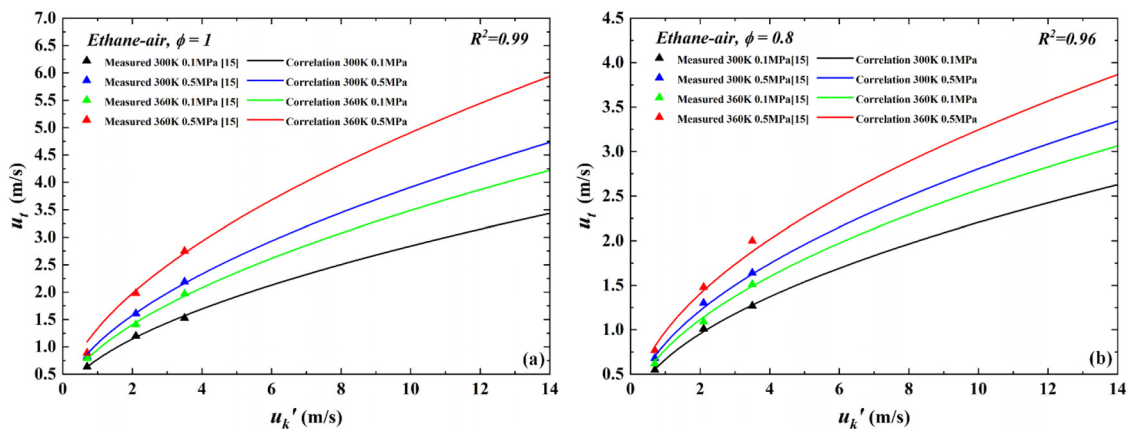

FIG. 1. Comparison of measured and correlated turbulent burning velocities for ethane–air at equivalence ratio $\phi = 1.0$ and 0.8 under various temperatures, pressures, and effective RMS turbulent velocities.

TABLE II. Physical parameters of ethane–air with $\phi = 1.05$ and 0.8 used in simulation.

Fuel	Ethane–air	
Equivalence ratio	1.05	0.8
Temperature (K)	300	300
Pressure (MPa)	0.1	0.1
Laminar burning velocity[19] (m/s)	0.407	0.297
Prandtl number	0.807	0.806
Kinematic viscosity (m²/s)	1.51×10^{-5}	1.53×10^{-5}
Unburned density (kg/m³)	1.175	1.174
Burned density (kg/m³)	0.149	0.169
Thermal diffusivity (m²/s)	1.87×10^{-5}	1.9×10^{-5}

The findings, as depicted in Fig. 1, demonstrate that the u'_k significantly influences the magnitude of u_t, showing a proportional increase with u'_k. This trend is explained by the increased wrinkling of the flame front area as u'_k increases, which in turn elevates the burning velocity. Additionally, an increase in initial temperature and pressure has been observed to further enhance u_t. This enhancement is attributed to the elevated heat release rate, which amplifies the reactivity of the mixtures. Furthermore, reducing the equivalence ratio from 1.0 to 0.8 results in a decrease in turbulent burning velocity under the same conditions of temperature, pressure, and u'_k, due to the diminishing effect of chemical kinetics on the burning velocity, potentially leading to flame quenching.

D. Boundary conditions and mesh setup

In the simulation, the focus is on two ethane–air mixture cases with equivalence ratios of 1.05 and 0.8. The 1.05 ratio aligns with the Shell experimental setup described in Ref. 2. Fuel and air are uniformly distributed throughout the channel, and both temperature and pressure meticulously match the experimental conditions, maintained at 300 K and 0.1 MPa, respectively. Table II below outlines the physical parameters and initial conditions. The unburned and burned densities, kinematic viscosity, thermal diffusivity, and Prandtl number for the ethane–air mixture are calculated using the GASEQ code.[23]

The simulation is conducted in a 2D channel, oriented along the x and y axes, with dimensions of 21 m in length (x axis) and 3 m in width (y axis). The configuration of the solid walls, cylindrical obstacles, and the ignition point is schematically depicted in Fig. 2. These dimensions are consistent with the central cross-section of the experimental setup illustrated in Ref. 2. Within the simulation, both the solid walls and cylindrical obstacles are modeled as non-slip, reflecting surfaces to mimic real-world physical barriers. Specifically, the solid wall extends along the bottom of the channel to simulate the ground, aligning with the experimental conditions.

The experimental setup by Shell, which is replicated in the simulation, used thin plastic sheets to enclose the ethane–air mixture. These sheets are known to rupture upon ignition due to the effects of burning gases and overpressure. The simulation abstracts away the influence of these plastic sheets on flame propagation, considering their destruction as the flame advances. The entire domain is filled with a stationary unburned ethane–air mixture and the boundary conditions on the left, top, and right sides of the domain are set as open, adhering to Neumann boundary condition. As illustrated in Fig. 3, the cylindrical obstacles are arranged in a uniform 8×16 grid, each with a 7 cm radius. The spacing between each row of obstacles is 35 cm, and the spacing between columns is 37 cm. The first row of obstacles is positioned 25 cm from the top wall, and the first column is 100 cm from the left wall. These setups are consistent with the central cross-section of the experimental setup described in Ref. 2.

Due to limited computing resources, it is challenging to conduct large-scale 3D simulations of flame propagation and transition to detonation. Consequently, a 2D simulation approach, similar to that employed in previous studies,[6–12] has been adopted. The study by Xiao and Oran,[24] which employed a rectangular domain with circular obstacles for 2D numerical simulations, is analogous to the configuration in the current work. The results from these 2D simulations show good agreement with 3D experimental observations in terms of flame acceleration and detonation propagation. However, Howarth et al.[25] noted that during the early stages of flame propagation post-ignition, flames in 3D experiments expand spherically, while 2D simulations depict cylindrical propagation. It is important to note that these early stage flame propagation are not the primary focus of this study.

This simulation employs AMR from level 1 to level 4, specifically automatically refines regions with physical changes including variations in density, pressure, and progress variables. This refinement specifically targets areas such as the flame front, baffles, and wall areas. This strategy helps in maintaining computational efficiency while
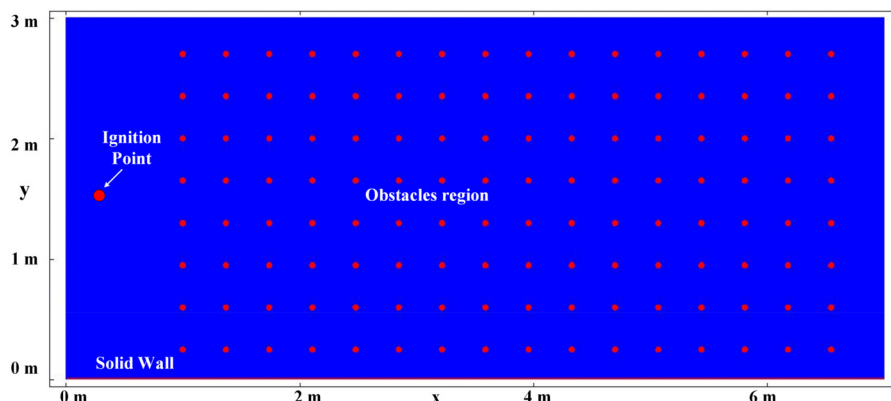
FIG. 2. Schematic configuration of simulation setup: Solid wall, obstacles region and ignition point.
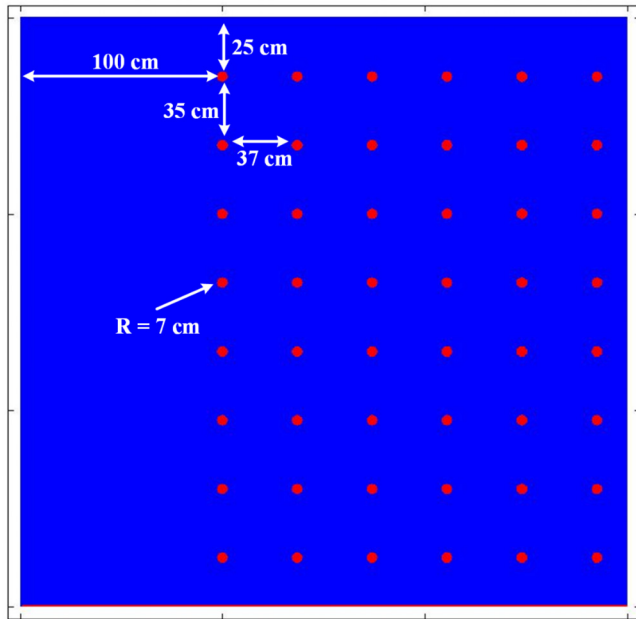
FIG. 3. Location of obstacles in simulation setup.

ensuring detailed resolution where it matters most. The differences between mesh levels 1 through 4 in the burned region are illustrated in Fig. 4, and detailed mesh information is provided in Table III below.

The mesh is configured in a square shape, and the maximum skewness values at levels 3 and 4 are less than 0.1. The average y^+ value selected as the mean near the fifth row of obstacles and the Courant number is consistently set at 0.3 across all cases. The minimum average y^+ near the obstacle area in current simulation is about 3.3, and the average y^+ value is a function with the cell size and from the best fitting can be expressed as follows:

$$y^+ = 0.264x^{-0.836}, \qquad (16)$$

where x represents the cell size with unit in meter.

The numerical study by Mirmotahari *et al.*[26] on wind turbines showed that simulations of wind turbine blades operating in conditions of relatively low turbulence and low Reynolds numbers required

a y^+ value around 1. In contrast, the current simulations involve turbulent flame propagation in subsonic flows (speeds exceeding 300 m/s) and detonation in supersonic flows (speeds over 1800 m/s), where higher levels of turbulence and Reynolds numbers prevail. These conditions suggest that an average y^+ value of 3.3 is suitable for effectively addressing both the buffer layer and the viscous sublayer.

At the level 1 mesh configuration, the cell size is set to 1 cm, matching the initial turbulent length scale with a resolution of two cells. This configuration yields a total cell count of approximately 630 000 for the entire channel. Progressing to level 2, the mesh resolution increases to double the cell density, reducing the cell size to 0.5 cm. This adjustment allows for the turbulent flame thickness to be spanned by at least four cells, raising the total cell count to approximately 2 520 000. The level 3 mesh further reduces the cell size to 0.25 cm, aligning with the requirement to resolve the initial turbulent flame thickness with at least eight cells. The highest resolution, level 4 mesh, decreases the cell size to 0.125 cm. Computations are performed on the Leeds ARC 4 high-performance computing cluster.

III. RESULTS AND DISCUSSION

A. Near stoichiometric ethane–air mixture

In the present study, the level 4 AMR is applied and the configuration of channel shown in Fig. 2 is used to simulate the flame propagation in the channel with obstacles. It is noticed that the length of the channel in this simulation is 21 m and the domain with length from 0 to 7 m is selected with the time sequences of reaction progress variable field crossing the obstacles region are shown in Fig. 5 where time representing the time after the ignition triggered. The red area represents the burned gases, while the blue area represents the unburned gases. At the beginning a spherical laminar flame with 5 cm radius expands freely outwards, as shown at t = 13.2 ms. As the flame passes crossing the obstacles at t = 37.3 ms, the flame front starts to wrinkling and the propagation speed is accelerated due to the increasing turbulent kinetics energies and thus the turbulent burning velocity. Eventually transition to detonation at t = 54.5 ms as flame approaches 6 m.

Figure 6 shows the flame front speed in relation to the flame front position (a), and both the flame front speed and position against with time (b). It is observed that during the initial phase of laminar flame propagation, the acceleration remains relatively slow, maintaining a low speed of approximately 30 m/s. This is explained by Refs. 27 and 28 in the early flame acceleration stage of laminar flame in a channel mainly originates from the thermal expansion of hot products of
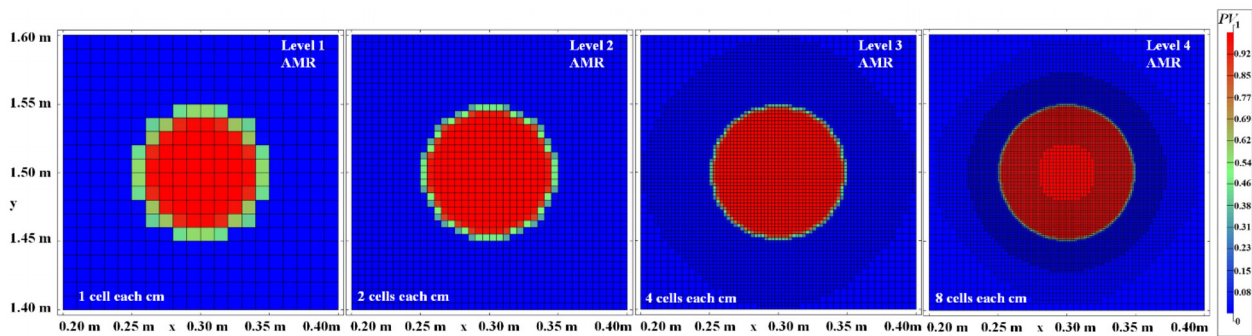

FIG. 4. Comparison of level 1, 2, 3, and 4 AMR computational domain showing the adaptive mesh refined for flame.

TABLE III. Adaptive mesh refinement details for the current simulation.

AMR mesh level	Level 1	Level 2	Level 3	Level 4
Number of elements (10^3)	630	2520	3000–8000	3200–22 000
Mesh size near the walls (cm)	1	0.5	0.25	0.125
The first near-wall computational cell distance (cm)	0.5	0.25	0.125	0.0625
Average y^+ for the unburned mixtures near obstacle	15	7.8	4.5	3.3
Maximum skewness	0	0	Less than 0.1	Less than 0.1
Mesh shape	Square	Square	Square	Square
Courant number	0.3	0.3	0.3	0.3

combustion. Once the flame starts to entrain the obstacles region at position of 1 m, a rapid acceleration of the flame front speed is observed. This speed increases from 40 m/s to approximately 750 m/s at position of 5.2 m, marking almost the end of the obstacle's region. DDT occurs when the flame approaches to 5.5 m, approximately 54.4 ms following ignition. Subsequently, it maintains a supersonic propagation speed of approximately 1830 m/s closing to the Chapman–Jouguet (C–J) detonation speed. This observed acceleration of the flame through the obstacles within the channel and DDT aligns with the findings from experimental studies[28] and simulation research.[10,29]

Figure 7 provides further insights into the effects of gas compression ahead of the flame and the enhancement of turbulence levels as the flame accelerates across the obstacle area. It illustrates this by depicting the temperature field in the left column and the turbulent kinetic energy field in the right column at three time points: 34.1, 48.7, and 54 ms. For the turbulent kinetic energy field, k, the scale ranges from 0 (represented in blue) to a maximum of 14 300 m^2/s^2 (indicated in red). At t = 34.1 ms, Fig. 7 shows only a small vortex area with low turbulent kinetic energy values, located exclusively around obstacles ahead of the flame. This localized turbulence is primarily generated due to the dynamic interaction between the flame front and the obstacles. As the flame continues propagating across the numerous obstacles, there is a conspicuous amplification in vortex characteristics, including an escalation in size, a proliferation in quantity, and a surge in strength, observable within the timeframe from t = 48.7 to t = 54 ms.
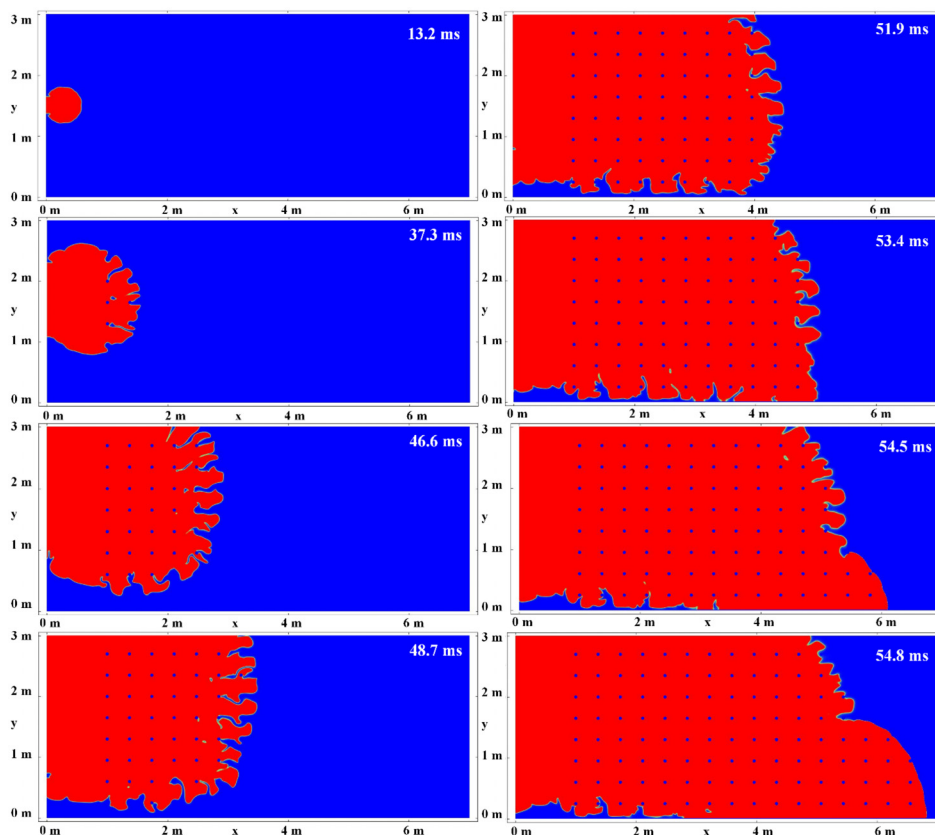

FIG. 5. Time-sequence of progress variable field demonstrating the turbulent flame acceleration and its interaction with the cylindrical obstacle rows.
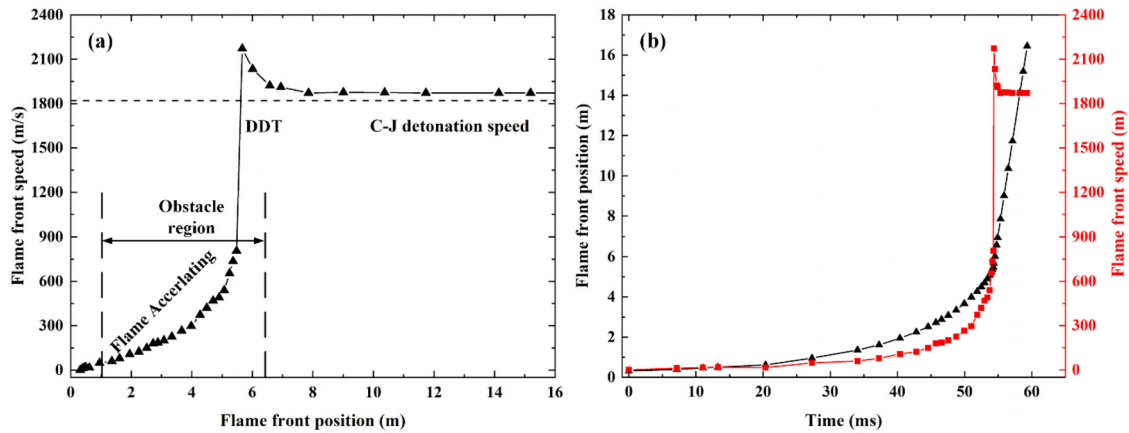
FIG. 6. The simulated flame front speed as a function of flame front position (a) and flame front position/speed with time for ethane–air with $\phi = 1.05$.

The generation of turbulent vortex ahead of flame play a key role in flame acceleration in the channel, and this is supported with the numerical study of Refs. 6, 7, 30, and 31 and experimental study of Ref. 32. Di Sarli et al.[32] employed particle image velocimetry (PIV) techniques in the channel with baffles to examine the interaction between the flame and turbulent vortex. Their result showed that the turbulent vortex wrinkling the flame surface increasing the flame surface area thus accelerating the flame propagation speed. Bradley et al.[31] in the numerical study emphasized the role of turbulence accelerating the flame in the channel due to the increasing of turbulent burning velocity. As the Eq. (15) suggests, an increase in turbulent kinetics energy results in a corresponding rise in u'_k, consequently boosting the value of u_t and flame propagation speed. Such rising further enhance the interaction between the flame and obstacles, resulting in a greater quantity of turbulent vortices with heightened kinetic energy, thereby further increasing the value of u_t. This is the first feedback mechanism leading to the high flame speed.

The left column of Fig. 7 displays the temperature field, clearly illustrating the compression effects on the flow ahead of the flame. The temperature scale is set from 300 to 600 K. At t = 34.1 ms, the compression effects on the gas are minimal due to the low velocity of the gas in front of the flame, as evidenced by the temperature staying roughly 340 K ahead of the flame front. However, as the flame accelerating, the rising of gas velocity ahead of the flame enhances the compression effects. By t = 48.7 ms, these enhanced compression effects elevate the unburned gas temperature to around 415 K. This phenomenon serves as the second feedback mechanism that leads to high flame speed. As proposed by Bradley et al.,[31] during flame acceleration, high-speed gas ahead of flame, compressing the unburned mixtures to higher temperature and pressure. As indicated by Eq. (10), increases in both temperature and pressure raise the value of u_t, consequently increasing the speed of flame propagation. The average temperature and turbulent kinetic energy ahead of the flame, prior to DDT, are depicted in Fig. 8. This average covers the area from the flame front to
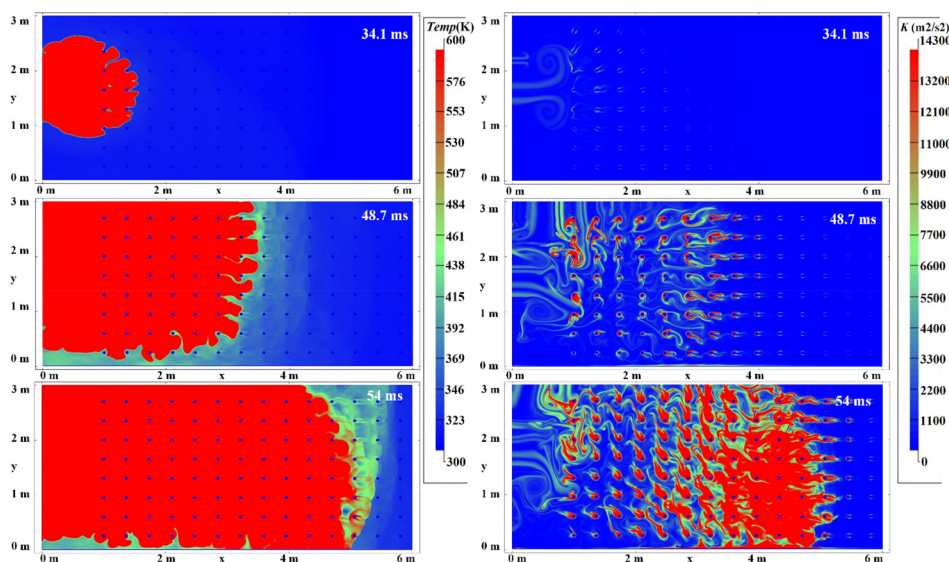
FIG. 7. Time-sequence of temperature (left) and turbulent kinetic energy field (right) for ethane–air with $\phi = 1.05$ as flame crossing the obstacles region.
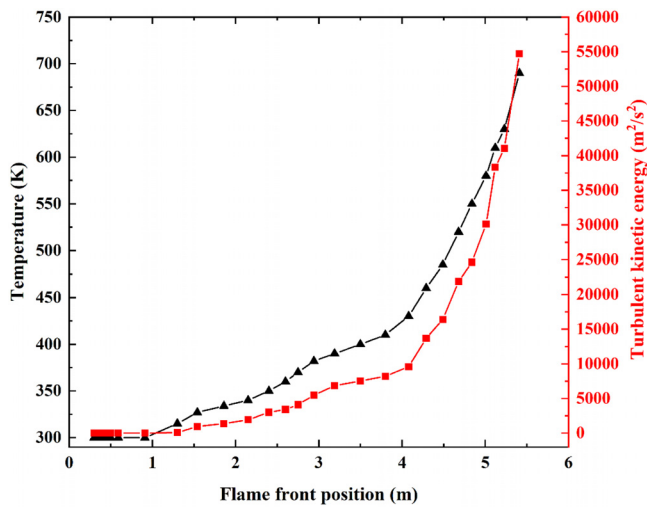
FIG. 8. The simulated average flame front temperature and turbulent kinetics energy by flame front position for ethane–air with $\phi = 1.05$.

20 cm ahead of the flame. As the flame traverses the obstacle-laden regime, both the temperature and turbulent kinetic energy increase, primarily due to the acceleration of flame propagation speed. This acceleration intensifies the compression effects and generates more turbulence. Notably, at the onset of DDT, the average compressed temperature and turbulent kinetic energy are approximately 675 K and 55 000 m^2/s^2, respectively.

In this simulation, DDT was observed at 54.4 ms after ignition, as the flame front reached 5.4 m. This phenomenon is substantiated by the measured parameters of density, temperature, and pressure (illustrated in the left, center, and right columns, respectively) recorded at times t = 54.4, 54.5, and 54.8 ms along the x axis, spanning 4–7 m, as shown in Fig. 9. At t = 54.4 ms, the shock wave is generated ahead of the flame front, compressing the surrounding unburned mixture. The localized compression peaks at a temperature of 1250 K, a pressure of 3 MPa, and a density of 12.9 kg/m^3, particularly around the lower column baffle. These conditions could lead to autoignition and subsequent transition to detonation, facilitated by the coupling of the flame front with the shock wave. Furthermore, evidence of DDT is provided by the flame front speed, which escalates rapidly from 750 m/s to maximum 2150 m/s within the 54.4–54.5 ms timeframe, stabilizing around
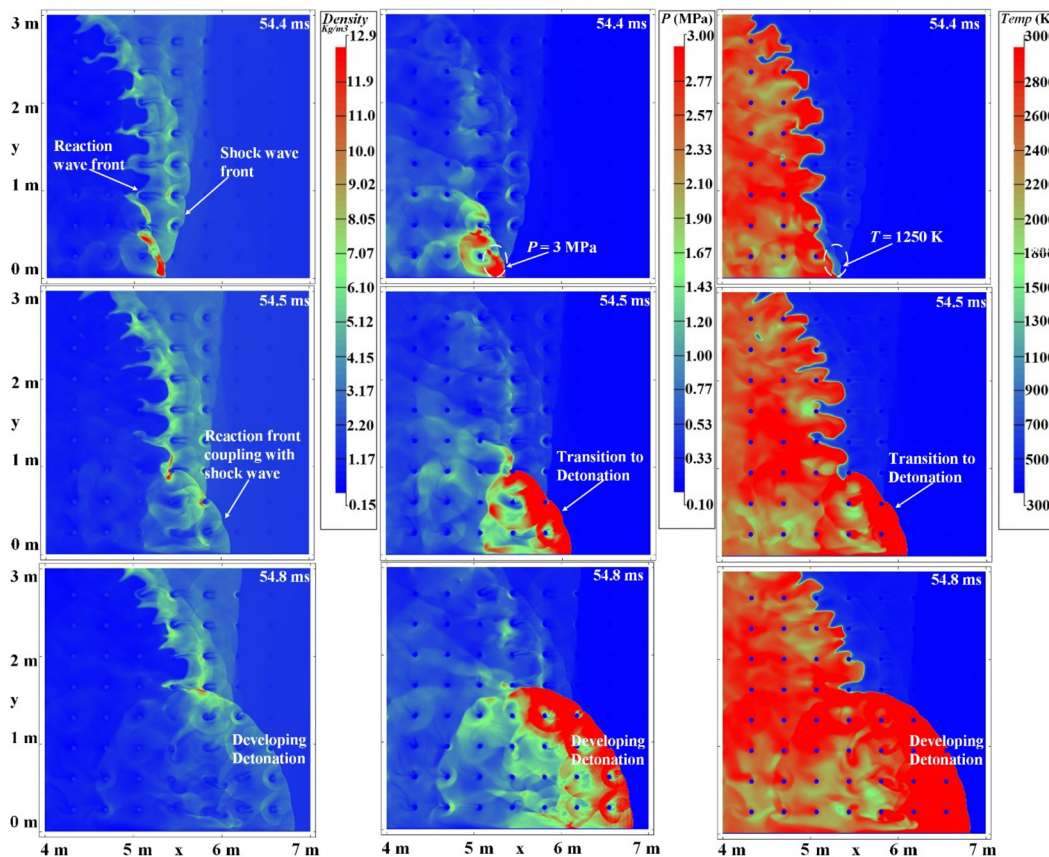

FIG. 9. Time-sequence of density (left), pressure (mid), and temperature (right) field showing the transition to detonation for ethane–air with $\phi = 1.05$.
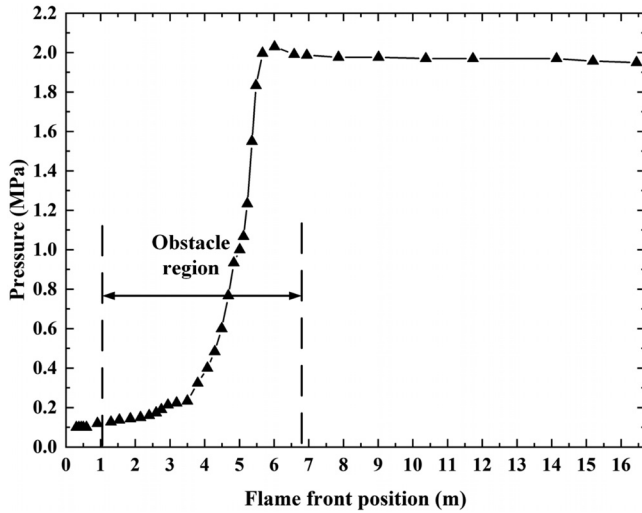
FIG. 10. The simulated average flame pressure against with flame front position for ethane–air with $\phi = 1.05$.

1830 m/s, approaching the C–J detonation speed. This increase in speed beyond the C–J threshold confirms the successful transition to detonation, as noted in Refs. 30 and 33. Subsequently, a steady detonation wave is established by t = 54.8 ms, as depicted in Fig. 10. This wave consistently maintains a speed of about 1830 m/s as it progresses toward the right end of the channel.

Moreover, the average flame front pressure is illustrated in Fig. 10 below. In the obstacle region, there is an incremental increase in pressure, demonstrating the growing strength of the compressive effects. Simultaneously, a sudden surge to a peak value of 2.1 MPa in pressure coincides with the occurrence of DDT. Following this peak, the shock wave, in conjunction with the detonation wave, maintains a steady pressure of approximately 1.9 MPa, indicative of steady-state detonation propagation. Such overpressure, measuring 19 times atmospheric pressure, this level of overpressure can also lead to severe injuries or

fatalities among people in the vicinity, as well as widespread disruption of nearby residential and industrial areas.

B. Lean ethane–air mixture

The second simulation presented in this study examines an ethane–air mixture with an equivalence ratio of 0.8 to explore the influence of the equivalence ratio on flame acceleration and DDT. This simulation employed the same setup as depicted in Fig. 2, utilizing level 4 AMR. The physical and combustion characteristics pertinent to this ratio are detailed in Tables I and II. In comparison to the near-stoichiometric mixture, this lean mixture possesses a reduced laminar burning velocity, specifically 0.297 m/s in contrast to 0.407 m/s, and displays a diminished response to increases in temperature, which is evident from the lower β_T and β_{Tl} temperature constant factor. Overall, from the turbulent burning velocity shown in Fig. 2, under the same conditions of temperature, pressure, and turbulence, the turbulent burning velocity for the ethane–air mixture with $\phi = 1.05$ is significantly higher than for $\phi = 0.8$. This contributes to the lower turbulent flame propagation speed observed in the simulation.

Figure 11 illustrates the flame front speed against with position (a), as well as the flame speed and position against with time (b) for an ethane–air mixture with $\phi = 0.8$. As the flame front traverses the obstacle regime, its speed accelerates, reaching a peak of approximately 620 m/s at the 7 m mark, which marks the end of the obstacle region. This peak velocity, which is thrice less than the C–J detonation speed, indicates that the flame does not undergo a transition to detonation. After this region, the flame front speed begins to diminish as the flame progresses further. Meanwhile, as illustrated in Fig. 6, the flame in the ethane–air mixture with a $\phi = 1.05$ propagates approximately 1.4 times faster through the obstacle region than with $\phi = 0.8$, and transitions to detonation at around the 5.7 m. The observed pattern of flame speed increasing and then decreasing in the $\phi = 0.8$ case is elucidated in Fig. 11, which shows turbulent kinetic energy accumulating as the flame interacts with the obstacles. However, once the flame front exits the obstacle area and the interaction diminishes, a decrease in turbulent kinetic energy occurs, leading to a diminished turbulent flame propagation speed.
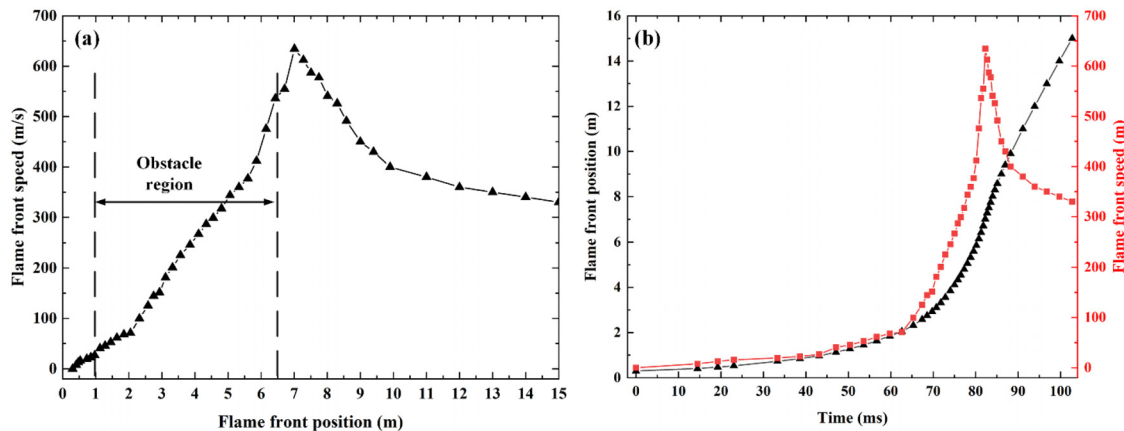

FIG. 11. The simulated flame front speed as a function of flame front position (a) and the flame front position/speed with time (b) for ethane–air with $\phi = 0.8$.
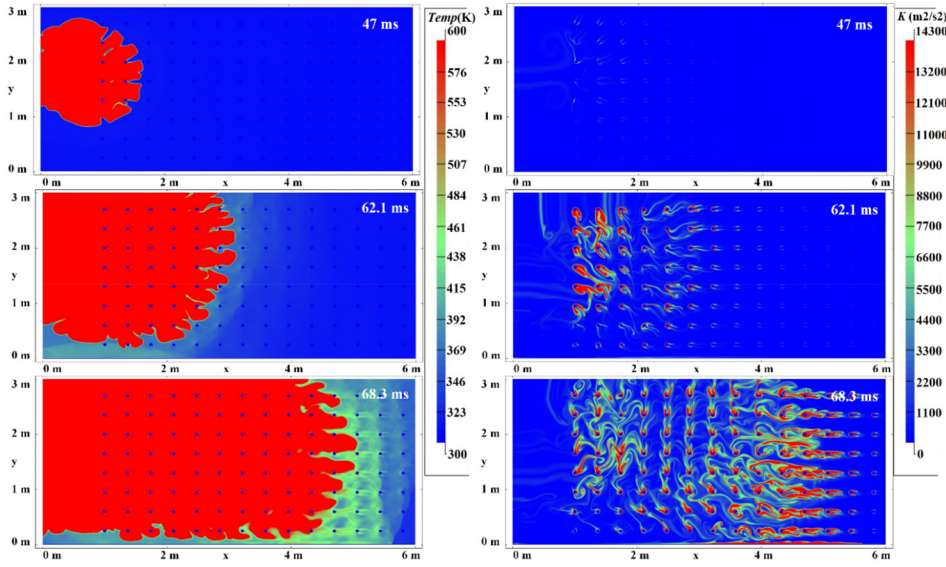
FIG. 12. Time-sequence of temperature (left) and turbulent kinetic energy field (right) for ethane–air with $\phi = 0.8$.

Figure 12 displays the temperature and turbulent kinetic energy distribution for $\phi = 0.8$, respectively, as the flame front reaches approximately 1.5, 3, and 5 m, using the same flame position and scale as in Fig. 7 for $\phi = 1.05$, for comparison purposes. Overall, Fig. 7 shows that both the magnitude and the area of high temperature and turbulent kinetic energy ahead of the flame for $\phi = 0.8$ are lower compared to $\phi = 1.05$, indicating weaker compressive and turbulent accelerating effects on flame propagation. The quantified average temperature and turbulent kinetic energy, plotted against the flame front position for the $\phi = 0.8$ case, are shown in Fig. 13. The peak values recorded are 525 K for temperature and 34 000 m^2/s^2 for turbulent kinetic energy, which are significantly lower than the DDT threshold values of 675 K and 55 000 m^2/s^2 observed for $\phi = 1.05$. Furthermore, Fig. 1 indicates that the ethane–air mixture with $\phi = 0.8$ needs more turbulence to reach the u_t required for DDT compared to $\phi = 1.05$, suggesting that higher temperature and turbulent kinetic energy thresholds are necessary for $\phi = 0.8$ to achieve DDT. This discrepancy underscores the findings of Bradley et al.,[31] noting that leaner mixtures exhibit weaker turbulent acceleration effects and are less likely to undergo DDT. In contrast, stoichiometric mixtures, with higher u_t, tend to reach DDT conditions more readily.

In Fig. 14 below, the flame pressure for an ethane–air mixture with an $\phi = 0.8$ increases in the obstacle region, culminating in a maximum of 0.65 MPa at the 7 m mark, which marks the end of this region. This peak pressure is contrasted with the 2.1 MPa observed in Fig. 10, where an acoustic wave interacts with the flame front at $\phi = 1.05$. The comparison indicates that under the conditions in Fig. 14, there is no transition to detonation. As the flame exits the
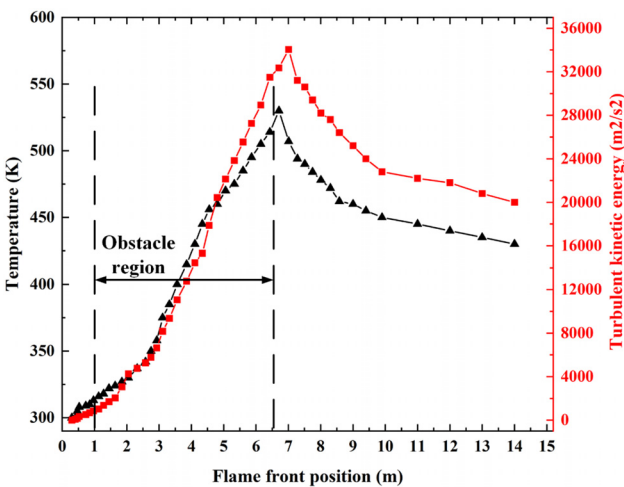
FIG. 13. The simulated average flame front temperature and turbulent kinetics energy by flame front position for ethane–air with $\phi = 0.8$.
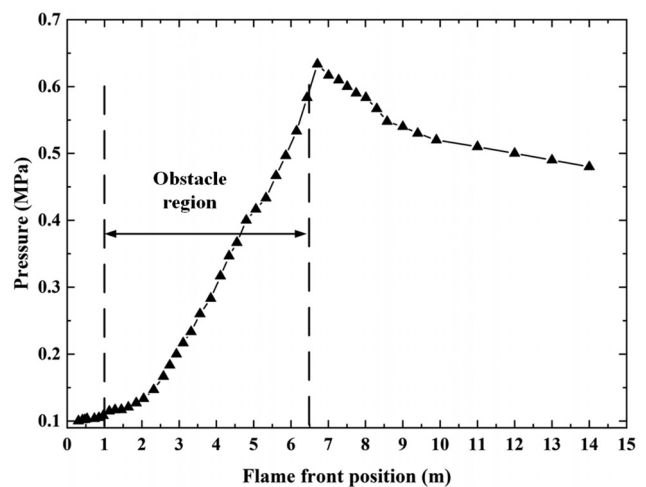

FIG. 14. The simulated average flame pressure against with flame front position for ethane–air with $\phi = 0.8$.

obstacle region, the pressure decreases due to the deceleration of the flame front propagation speed.

C. Mesh refinement test and validated with experimental results

This study conducted a numerical mesh resolution test across four distinct grid resolutions to validate simulation accuracy and improve computational efficiency. Figure 15(a) presents the flame front speed for an ethane–air mixture with an $\phi = 1.05$ across these resolutions. As the mesh resolution increases, a noticeable decrease and convergence in flame propagation speed are observed, particularly from level 3 to level 4 AMR, where speeds are nearly identical. This trend highlights the critical role of mesh cell quantity in accurately resolving flame thickness and its impact on flame propagation speed. For the level 4 AMR, at least 16 mesh cells are used to resolve the turbulent integral length scale. DDT occurred at different x-axis positions for each AMR level. Specifically, for level 1 AMR, the reaction wave reached an x-axis position of 4 m, while for levels 2, 3, and 4 AMR, it occurred at 4.8, 5.3, and 5.5 m, respectively. Following the DDT, all levels maintained a consistent detonation propagation speed of approximately 1830 m/s.

Figure 15(b) compares the flame front speeds from the level 4 AMR simulation with those experimental measurements in Ref. 2, utilizing data captured by a high-speed camera (depicted as a black dashed line with symbols) and a pressure sensor (depicted as a blue dashed-dotted line with symbols). Although the simulation results show the flame front speed to be slightly higher, they generally align well with the observed data from the high-speed camera as the flame progresses through the obstacle region.

According to data from the high-speed camera, the deflagration-to-detonation transition occurs at an x-axis position of 5.7 m, reaching a peak speed of 2100 m/s, indicative of an overdriven detonation. This is followed by a sudden decrease in speed to approximately 1350 m/s, which is below the C–J detonation speed. This drop in speed is most likely due to a measurement error, as it unexpectedly falls below the established C–J threshold. This anomaly at the final measurable point suggests a transient recording error at high speeds. Supporting these observations, the review study by Oran et al.[6] reported that the initial

formation of a detonation wave is typically characterized by an overdriven state due to complex interactions between the shock wave and the reactive wave front. Subsequently, there is a slight decrease in the propagation speed, which then stabilizes near the C–J detonation speed, maintaining stability and continuing to propagate until the fuel–air mixture is fully consumed. In contrast, the simulation indicates the DDT occurring at the same x-axis position with high-speed-camera measurements but reaching a higher peak speed around 2150 m/s with overdriven detonation and subsequently maintaining a stable propagation speed close to the C–J detonation speed. Overall, the propagation speed of the flame front in this simulation closely matches the experimental data.

Note that measurements of flame front speed using a high-speed camera are generally considered more accurate because it directly measures the speed of the flame front. In contrast, the flame speed captured by pressure sensors may exhibit oscillations, particularly when the flame is within the 4–6 m range. This occurs because pressure sensors measure overpressure during flame propagation in combustion systems, which can be subject to noise and oscillatory behavior, potentially introducing experimental errors. Therefore, the velocity data from flame propagation measured by these sensors should be considered as auxiliary verification rather than primary evidence.

D. Detonation peninsula, ξ and ε for ethane–air mixtures

In this simulation, it is significant to note that DDT occurs in a localized area near the lower solid wall. This observation is consistent with the research conducted by Oran et al.[6] and Bradley et al.,[31] which indicates that DDT tends to occur in regions where both temperature and pressure are sufficiently high to trigger autoignition hot spot and subsequently, detonation. Specifically, the conditions observed at $t = 54.4$ ms in Fig. 9, with the maximum localized temperature and pressure at 1250 K and 3 MPa, respectively, appear to be conducive for this transition. To further quantify these conditions for ethane–air, the ξ–ε detonation peninsula[17] is employed in this study. This detonation peninsula diagram classifies deflagration, subsonic autoignition, developing detonation, and thermal explosion based on the values of the dimensionless parameters ξ and ε. This method has successfully
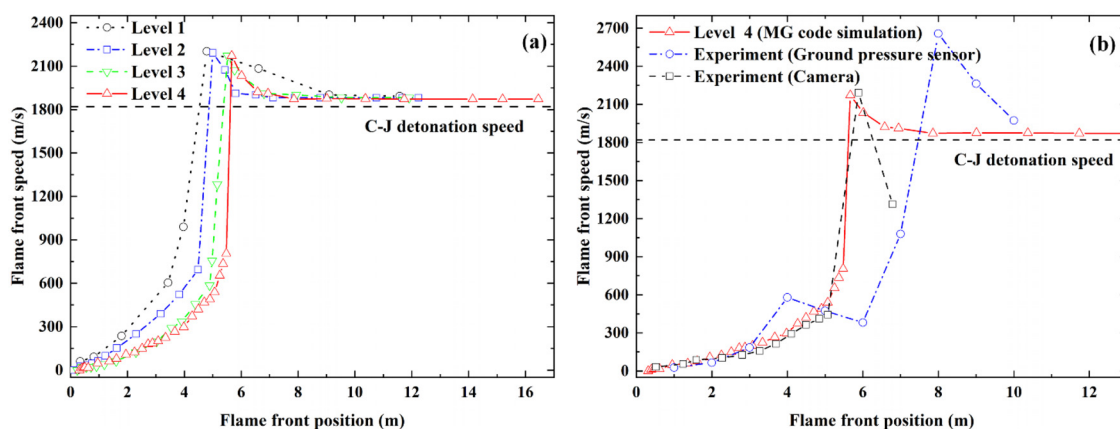

FIG. 15. Flame front speed against with flame front position for level 1, 2, 3, and 4 AMR (a) and simulation speed compared with the experimental speeds (b).

12 September 2024 11:09:58

quantified DDT in various fuels such as iso-octane,[34] coal-based naphtha,[35] n-butanol,[36] and methanol.[37]

The first dimensionless parameter ξ is relevant to the development of detonation and indicates the proximity of the autoignitive wave propagation transition to detonation. It is defined by the ratio of local acoustic velocity to the autoignitive velocity:

$$\xi = \frac{a}{u_a}, \tag{17}$$

where a is the acoustic velocity through the reactive mixture and u_a is the hot spot autoignitive velocity. The latter can be further defined as

$$u_a = \frac{\partial r}{\partial \tau_i} = \left(\frac{\partial r}{\partial T}\right)\left(\frac{\partial T}{\partial \tau_i}\right). \tag{18}$$

In this context, $\frac{\partial T}{\partial \tau_i}$ is the inversely proportional to the gradient of ignition delay time with temperature and $\frac{\partial T}{\partial r}$ is the temperature gradient alone the autoignition hot spot with the radius and following the previous study in Refs. 34–38, a constant $\frac{\partial T}{\partial r} = -2$ K/mm is applied. Another dimensionless parameter, ε, reflects the rate of energy input from a reactive hot spot with radius r_0, into an autoignitive flow, written as

$$\varepsilon = \frac{r_0}{a\tau_e}, \tag{19}$$

where r_0 is the hot spot radius, and based on numerous observations from engine and rapid compression machine experiments,[34,39] an average hot spot size of 5 mm has been observed and selected for use in this study. The ratio of r_0 over a indicates the residence time of acoustic wave inside the hot spot. Lutz et al.[40] introduced the concept of chemical excitation time, τ_e, which refers to the period during which exothermic chemical reactions accelerate and rapidly release thermal energy. It is the time interval from the point with 5% of the maximum total volumetric heat release rate to the attainment of that maximum value. The ethane oxidation kinetics embedded in the detailed Aramco MECH 1.3[41] was employed here to calculate the τ_i and τ_e for ethane–air under closed homogeneous batch reactor conditions using the

CHEMKIN-PRO software.[42] This kinetics[41] is reliable since it has been validated using the ignition delay time of ethane–air mixtures from shock tube experiments conducted over a wide range of temperatures (833–2500 K), pressures (0.06–26 MPa), and equivalence ratios (0.06–6).

The computed τ_i and τ_e of ethane–air with $\phi = 1.05$ and 0.8 as a function of the inverse temperature $1000/T$ at pressure 1–3 MPa for ethane–air and correlations are presented in Figs. 16 and 17. A correlation of τ_i and τ_e for ethane–air as a function of T and P proposed by Kalghatgi and Bradley[39] is adopted here:

$$\tau_i, \tau_e = A \times e^{(B/T)} \times P^C \times \phi^D, \tag{20}$$

where τ_i in ms, τ_e in μs, T is in K, and P is in MPa. The partial derivative of Eq. (20) with respect to temperature yields Eq. (21),

$$\partial \tau_i / \partial T = B \times \tau_i / T^2. \tag{21}$$

To align the computed τ_i and τ_e in Figs. 16 and 17, the multiple-regression method is used to determine the constants A, B, C, and D in Eqs. (20) and (21), as detailed in Table IV. For a thorough investigation of the impact of temperature, pressure, and equivalence ratio on the transition of ethane–air to detonation in open space, the temperature and pressure scales extend up to 1300 K and 3 MPa, respectively. Overall, increases in temperature and decreases in pressure both reduce τ_i and τ_e, due to heightened reactivity. Comparatively, ethane–air mixtures with $\phi = 0.8$ exhibit longer τ_i and τ_e values than those with $\phi = 1.05$, although the differences are not significant.

As seen in Fig. 18, the impacts of temperature (ranging from 930 to 1300 K) and pressure (varying between 1 and 3 MPa) on the values of ξ and ε on the detonation peninsula diagram are depicted. The transition to detonation occurred within the area delineated by the dashed lines, marked as developing detonation. It is observed that temperature significantly influences the decline in ξ, while pressure dominates the increase in ε. Both increasing in temperature and pressure will lead to the decreasing ξ of and increasing of ε indicating the increasing heat release rate from hot spot. For an ethane–air mixture with $\phi = 1.05$, the conditions for entering the detonation peninsula are marked by specific temperature and pressure thresholds. At 1 MPa, the
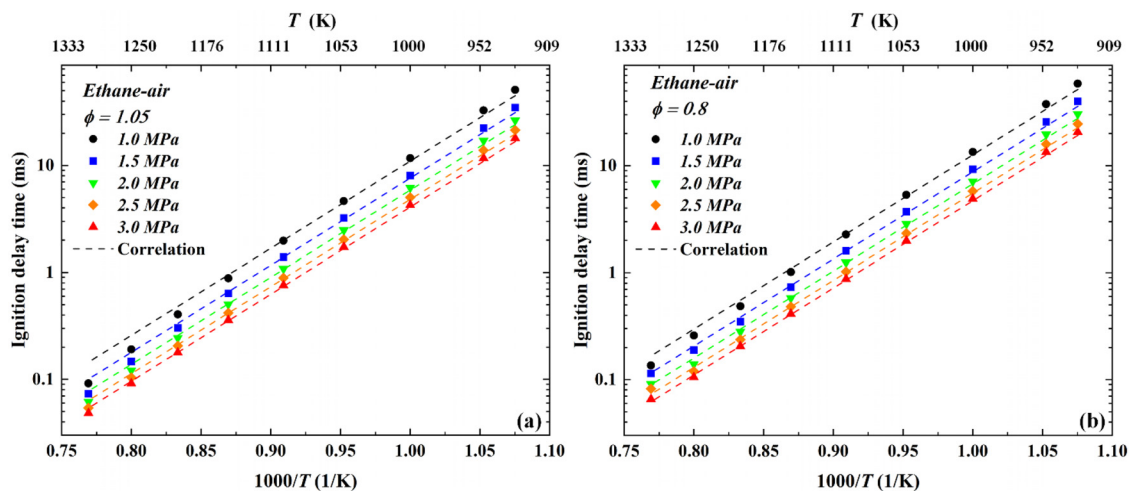

FIG. 16. Chemical kinetic (symbols) and correlation values (dashed line) of ignition delay time for ethane–air with $\phi = 1.05$ and 0.8 at pressure from 1.0 to 3.0 MPa.
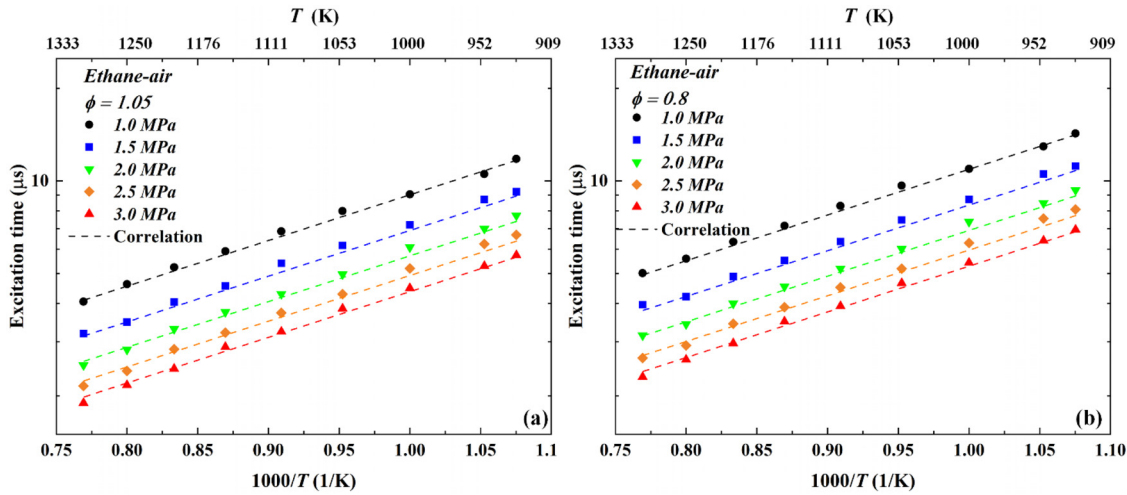
FIG. 17. Chemical kinetic and correlation values of excitation time for ethane–air with $\phi = 1.05$ at pressure from 1.0 to 3.0 MPa.

TABLE IV. Constants A, B, C, and D for τ_i and τ_e in ethane–air.

	τ_i	τ_e
A	7.8×10^{-8}	0.29
B	18740	3414
C	-0.9	-0.66
D	-0.6	-0.84

temperature required is 1250 K, while at higher pressures of 2 and 3 MPa, the temperature threshold decreases to 1200 and 1170 K, respectively. For the ethane–air mixture with $\phi = 0.8$, the conditions required to enter the detonation peninsula are similar to those for $\phi = 1.05$, indicating that the equivalence ratio does not significantly alter the conditions for the transition to detonation. Instead, temperature and pressure more dominantly influence this transition. The post-shock conditions represented in Fig. 9 at t = 54.4 ms, which

correspond to a temperature of 1250 K and a pressure of 3 MPa, are located in the developing detonation regime. This suggests that under such conditions, the triggering of a detonation becomes feasible.

IV. CONCLUSIONS

In this study, a framework for simulating large scale flame acceleration and DDT is presented. The approach utilizes a finite-volume MG code that integrates both the reaction progress variable and the k-ε turbulence model, along with a correlation for measured turbulent burning velocity. Using this framework, large-scale simulations of turbulent flame and DDT in ethane–air mixtures with $\phi = 0.8$ and 1.05 were conducted and compared with experimental results. For the ethane–air with $\phi = 1.05$, the flame propagates in a laminar fashion at speeds below 40 m/s until it encounters obstacles. These obstacles generate turbulence, wrinkling the flame front and increasing the turbulent kinetic energy. This results in a flame speed increase from 40 to 750 m/s with a maximum turbulent kinetic energy of 55 000 m^2/s^2. A strong shock wave then forms, compressing the unburned mixture
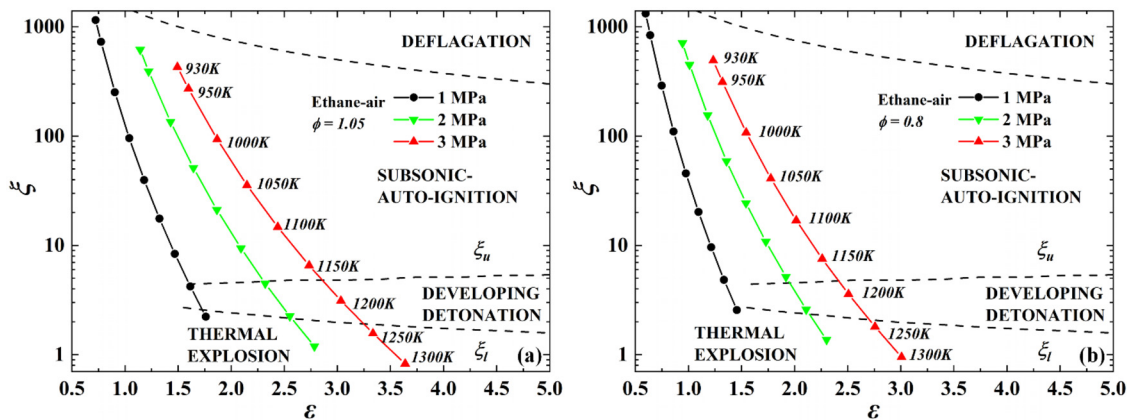

FIG. 18. Detonation peninsulas ξ–ε diagram for ethane–air with $\phi = 0.8$ and 1.05 at pressure of 1, 2, and 3 MPa, temperature from 930 to 1300 K.

and elevating its temperature and pressure, which triggers a transition to a stable and continuous detonation, with the flame propagation speed reaching 1830 m/s.

For the ethane–air mixture with $\phi = 0.8$, the flame speed accelerates to a peak of about 630 m/s at the end of the obstacle region. As the flame exits this area, a continuous decline in both flame speed and pressure is observed as it propagates further. No DDT is observed for $\phi = 0.8$, primarily due to the relatively low laminar and turbulent burning velocities and the slow flame acceleration, which lead to insufficient turbulent kinetic energy within the obstacle region. The ethane–air mixture with $\phi = 1.05$ was compared with Shell's large-scale experimental work, showing a good match in flame propagation speeds. Additionally, different levels of AMR testing were conducted, with satisfactory convergence in flame speed observed at level 4 AMR.

The dimensionless ξ–ε detonation peninsula method, paired with Aramco MECH 1.3 chemical kinetics mechanism, was used to quantify the conditions under which DDT would occur for ethane–air mixtures with $\phi = 0.8$ and 1.05. It was observed that the equivalence ratio does not significantly alter the required temperature and pressure for DDT, which remain at approximately 1200 K and 3 MPa, respectively. Based on the current numerical analysis, several insights are provided to prevent fire hazards and explosions: (i) Ethane is not a fuel that readily undergoes DDT in the current configuration of the rig. It requires near-stoichiometric conditions and a run-up distance of about 6 m in the obstacle region under the present setup. However, achieving a homogeneously stoichiometric mixture during an actual leak is difficult. (ii) Turbulence significantly contributes to creating conditions for DDT, especially in the obstacle region where the accumulation of turbulent kinetic energy leads to flame acceleration and rising pressures. (iii) For ethane–air mixtures, reducing the equivalence ratio from near-stoichiometric to 0.8 in the current setup can significantly decelerate the flame acceleration process and the generation of turbulent kinetic energy, effectively preventing DDT. (iv) Once formed, the detonation wave is strong and robust, continuously propagating. In contrast, a subsonic flame, deflagration, experiences a decline in propagation speed and pressure once it leaves the obstacle region and is no longer sustained by high turbulence levels, such flame decelerates to cloud fire.

Regarding future studies, it would be beneficial to develop the k-ω model within the MG code to enhance the treatment of wall boundary layers. While 2D simulations sometimes do not perfectly reflect the complexities of 3D experimental work, conducting small-scale 3D simulations of flame propagation and transition to detonation for ethane/air mixtures could provide valuable insights. Additionally, as indicated by the study of Xiao and Oran,[12] obstacles play a crucial role in accelerating turbulent flame propagation, and the distribution of these obstacles can significantly influence simulation results. Another promising area of research would be to explore the effects of the blockage ratio on turbulent flame propagation and the transition to detonation for ethane–air mixtures.

AUTHOR DECLARATIONS
Conflict of Interest

The authors have no conflicts to disclose.

Author Contributions

Jinzhou Li: Data curation (equal); Formal analysis (equal); Investigation (equal); Methodology (equal); Software (equal); Validation (equal); Visualization (equal); Writing – original draft (equal). **Sven Van Loo:** Conceptualization (equal); Funding acquisition (equal); Investigation (equal); Methodology (equal); Project administration (equal); Software (equal); Supervision (equal); Visualization (equal); Writing – review & editing (equal). **Junfeng Yang:** Conceptualization (equal); Funding acquisition (equal); Project administration (equal); Resources (equal); Supervision (equal); Writing – review & editing (equal). **Andrzej Pekalski:** Conceptualization (equal); Funding acquisition (equal); Project administration (equal); Resources (equal); Supervision (equal); Validation (equal); Writing – review & editing (equal).

DATA AVAILABILITY

The data that support the findings of this study are available from the corresponding author upon reasonable request.

REFERENCES

[1] S. Davis, E. Merilo, D. Engel, A. Ziemba, M. Pinto, and K. van Wingerden, "Large scale detonation testing: New findings in the prediction of DDTs at large scales," J. Loss Prev. Process Ind. **48**, 345–357 (2017).

[2] A. Pekalski, J. Puttock, and S. Chynoweth, "Deflagration to detonation transition in a vapour cloud explosion in open but congested space: Large scale test," J. Loss Prev. Process Ind. **36**, 365–370 (2015).

[3] M. P. Sherman, S. R. Tiezsen, W. B. Benedick, J. W. Fisk, and M. Carcassi, "Effect of transverse venting on flame acceleration and transition to detonation in a large channel," Report No. SAND-85-1386C (Sandia National Laboratories, 1985).

[4] R. J. Harris and M. J. Wickens, *Understanding Vapour Cloud Explosions: An Experimental Study* (Institution of Gas Engineers, London, 1989).

[5] B. J. Lowesmith, G. Hankinson, and D. M. Johnson, "Vapour cloud explosions in a long congested region involving methane/hydrogen mixtures," Process Saf. Environ. Prot. **89**, 234–247 (2011).

[6] E. S. Oran, G. Chamberlain, and A. Pekalski, "Mechanisms and occurrence of detonations in vapor cloud explosions," Prog. Energy Combust. Sci. **77**, 100804 (2020).

[7] E. S. Oran and V. N. Gamezo, "Origins of the deflagration-to-detonation transition in gas-phase combustion," Combust. Flame **148**, 4–47 (2007).

[8] B. Maxwell, A. Pekalski, and M. Radulescu, "Modelling of the transition of a turbulent shock-flame complex to detonation using the linear eddy model," Combust. Flame **192**, 340–357 (2018).

[9] A. M. Coates, D. L. Mathias, and B. J. Cantwell, "Numerical investigation of the effect of obstacle shape on deflagration to detonation transition in a hydrogen–air mixture," Combust. Flame **209**, 278–290 (2019).

[10] R. M. Woolley, M. Fairweather, S. A. E. G. Falle, and J. R. Giddings, "Prediction of confined, vented methane–hydrogen explosions using a computational fluid dynamic approach," Int. J. Hydrogen Energy **38**, 6904–6914 (2013).

[11]D. Liu, Z. Liu, and H. Xiao, "Flame acceleration and deflagration-to-detonation transition in narrow channels filled with stoichiometric hydrogen-air mixture," Int. J. Hydrogen Energy **47**, 11052–11067 (2022).

[12]H. Xiao and E. S. Oran, "Flame acceleration and deflagration-to-detonation transition in hydrogen–air mixture in a channel with an array of obstacles of different shapes," Combust. Flame **220**, 378–393 (2020).

[13]W. E. Liss, W. H. Thrasher, G. F. Steinmetz, P. Chowdiah, and A. Attari, "Variability of natural gas composition in select major metropolitan areas of the United States, final report, August 1990–February 1992," Report No. PB-92-224617/XAB (American Gas Association Labs., Cleveland, OH, 1992).

[14]J. Li, Y. Xie, M. E. Morsy, and J. Yang, "Laminar burning velocities, Markstein numbers and cellular instability of spherically propagation ethane/hydrogen/air premixed flames at elevated pressures," Fuel **364**, 131078 (2024).

[15]J. Li and J. Yang, "Experimental study on turbulent burning velocity of ethane and blends with hydrogen at elevated pressure".

[16]Y. B. Zeldovich, "Regime classification of an exothermic reaction with nonuniform initial conditions," Combust. Flame **39**, 211–214 (1980).

[17]L. Bates, D. Bradley, G. Paczko, and N. Peters, "Engine hot spots: Modes of auto-ignition and reaction propagation," Combust. Flame **166**, 80–85 (2016).

[18]S. A. E. G. Falle, "Self-similar jets," Mon. Not. R. Astron. Soc. **250**, 581–596 (1991).

[19]W. P. Jones and B. E. Launder, "The prediction of laminarization with a two-equation model of turbulence," Int. J. Heat Mass Transfer **15**, 301–314 (1972).

[20]M. Mehrpooya, F. Ghafoorian, and S. Farajyar, "3D-modeling of a coaxial borehole heat exchanger in Sahand Field, Northwest Iran considering the porous medium and presence of nanofluids," Iran. J. Chem. Chem. Eng. **42**, 11 (2023).

[21]C. A. Catlin, M. Fairweather, and S. S. Ibrahim, "Predictions of turbulent, premixed flame propagation in explosion tubes," Combust. Flame **102**, 115–128 (1995).

[22]D. Bradley, M. Lawes, K. Liu, and M. S. Mansour, "Measurements and correlations of turbulent burning velocities over wide ranges of fuels and elevated pressures," Proc. Combust. Inst. **34**, 1519–1526 (2013).

[23]See http://www.gaseq.co.uk, for C. Morley, "GASEQ: A chemical equilibrium program for Windows" (2005).

[24]H. Xiao and E. S. Oran, "Shock focusing and detonation initiation at a flame front," Combust. Flame **203**, 397–406 (2019).

[25]T. L. Howarth, E. F. Hunt, and A. J. Aspden, "Thermodiffusively-unstable lean premixed hydrogen flames: Phenomenology, empirical modelling, and thermal leading points," Combust. Flame **253**, 112811 (2023).

[26]S. R. Mirmotahari, F. Ghafoorian, M. Mehrpooya, S. Hosseini Rad, M. Taraghi, and M. Moghimi, "A comprehensive investigation on Darrieus vertical axis wind turbine performance and self-starting capability improvement by

implementing a novel semi-directional airfoil guide vane and rotor solidity," Phys. Fluids **36**, 065151 (2024).

[27]H. Xiao, D. Makarov, J. Sun, and V. Molkov, "Experimental and numerical investigation of premixed flame propagation with distorted tulip shape in a closed duct," Combust. Flame **159**, 1523–1538 (2012).

[28]V. Bychkov, V. Y. Akkerman, G. Fru, A. Petchenko, and L. E. Eriksson, "Flame acceleration in the early stages of burning in tubes," Combust. Flame **150**, 263–276 (2007).

[29]T. Pinos and G. Ciccarelli, "Combustion wave propagation through a bank of cross-flow cylinders," Combust. Flame **162**, 3254–3262 (2015).

[30]D. A. Kessler, V. N. Gamezo, and E. S. Oran, "Simulations of flame acceleration and deflagration-to-detonation transitions in methane air systems," Combust. Flame **157**, 2063–2077 (2010).

[31]D. Bradley, M. Lawes, and K. Liu, "Turbulent flame speeds in ducts and the deflagration/detonation transition," Combust. Flame **154**, 96–108 (2008).

[32]V. Di Sarli, A. Di Benedetto, G. Russo, S. Jarvis, E. J. Long, and G. K. Hargrave, "Large eddy simulation and PIV measurements of unsteady premixed flames accelerated by obstacles," Flow, Turbul. Combust. **83**, 227–250 (2009).

[33]L. Q. Wang, H. H. Ma, Z. W. Shen, and D. G. Chen, "Experimental study of DDT in hydrogen-methane–air mixtures in a tube filled with square orifice plates," Process Saf. Environ. Prot. **116**, 228–234 (2018).

[34]D. Bradley and J. Li, "Reaction propagation, leading to developing detonation, in a rapid compression machine," Combust. Flame **262**, 113331 (2024).

[35]J. Li, A. Lu, Y. Xie, J. Yang, and C. Zhang, "Auto-ignition characteristics of coal-based naphtha," Appl. Energy **359**, 122768 (2024).

[36]I. Gorbatenko, D. Bradley, and A. S. Tomlin, "Auto-ignition and detonation of n-butanol and toluene reference fuel blends (TRF)," Combust. Flame **229**, 111378 (2021).

[37]Y. Wang, Y. Qi, W. Liu, and Z. Wang, "Investigation of methanol ignition phenomena using a rapid compression machine," Combust. Flame **211**, 147–157 (2020).

[38]J. Li and J. Yang, "Analysis of super knock and detonation in a rapid compression machine," in Proceedings of the 29th ICDERS, Korea (2023).

[39]G. T. Kalghatgi and D. Bradley, "Pre-ignition and 'super-knock' in turbocharged spark-ignition engines," Int. J. Engine Res. **13**, 399–414 (2012).

[40]A. E. Lutz, R. J. Kee, J. A. Miller, H. A. Dwyer, and A. K. Oppenheim, "Dynamic effects of autoignition centers for hydrogen and $C_{1,2}$-hydrocarbon fuels," Symp. (Int.) Combust. **22**, 1683–1693 (1989).

[41]W. K. Metcalfe, S. M. Burke, S. S. Ahmed, and H. J. Curran, "A hierarchical and comparative kinetic modeling study of C_1–C_2 hydrocarbon and oxygenated fuels," Int. J. Chem. Kinetics **45**, 638–675 (2013).

[42]CHEMKIN-Pro 19.2, Reaction Design, San Diego, CA, 2017.